Quantitative Analysis and Computation of Two-Dimensional Bubble Columns

T.-J. Lin, J. Reese, T. Hong, and L.-S. Fan
Dept. of Chemical Engineering, The Ohio State University, Columbus, OH 43210

Experiments conducted quantify the macroscopic hydrodynamic characteristics of various scale 2-D bubble columns, which include dispersed and coalesced bubble regimes characterized by two flow conditions (4- and 3-region flow) with coherent flow structures. Hydrodynamic behavior is analyzed based on flow visualization and a particle image velocimetry (PIV) system. Columns operated in the 4-region flow condition comprise descending, vortical, fast bubble and central plume regions. The fast bubble flow region moves in a wavelike manner, and thus the flow in the vicinity of this region is characterized macroscopically in terms of wave properties. In columns greater than 20 cm in width, the transition from the dispersed bubble flow regime to the 4- and then to 3-region flow in the coalesced bubble regime occurs progressively with gas velocities at 1 and 3 cm/s, respectively. The demarcation of flow regimes is directly related to measurable coherent flow structures. The instantaneous and time-averaged liquid velocity and holdup profiles provided by the PIV system are presented in light of the macroscopic flow structure in various 2-D bubble columns. Numerical simulations demonstrate that the volume of fluid method can provide the time-dependent behavior of dispersed bubbling flows and account for the coupling effects of pressure field and the liquid velocity on the bubble motion. Comparison of computational results with PIV results for two different bubble injector arrangements is satisfactory.

Introduction

Experimental bubble column studies

Bubble columns are widely adopted in industry for chemical, petrochemical, biochemical, and environmental applications (Fan, 1989). Although there have been significant research efforts concerning the fundamental characteristics of bubble columns (Shah et al., 1982; Deckwer and Schumpe, 1987; Fan, 1989), the scale effects on the flow structure of the columns is still not fully understood. Tarmy and Coulaloglou (1992) indicated that the scale-up of bubble column reactors requires a knowledge of virtually all aspects of reaction engineering and the underlying core chemical engineering technologies. Sound understanding of the hydrodynamic behavior in bubble columns (e.g., the flow regimes, phase holdup, bubble characteristics, interfacial phenomena, backmixing, and interphase transport) is therefore clearly essential in designing and scaling up bubble column reactors.

Correspondence concerning this article should be addressed to L.-S. Fan.

There are three different flow regimes commonly identified in bubble column systems: dispersed bubble, churn-turbulent, and slugging (Muroyama and Fan, 1985). A gross circulating flow of liquid is observed for these systems under both the dispersed bubble and churn-turbulent (coalesced bubble) regimes (De Nevers, 1968; Freedman and Davidson, 1969; Hills, 1974). In general, the gross circulation comprises an upward flow in the column core and a downward flow along the wall with the inversion point (zero axial liquid velocity) located at about 0.5 to 0.7 radius of the column (Walter and Blanch, 1983). This nonuniform velocity distribution is significant in characterizing the column hydrodynamics, phase mixing characteristics, heat transfer, and mass transfer. Due to limitations in experimental techniques, most of the previous studies were concerned with the gross flow circulation in a bubble column rather than detailed local flow structure and its associated governing mechanisms.

Previous studies on the flow structures of bubble columns

have mostly involved measurement of the time/volume-averaged flow properties with the assumption that the flow is steady-state and one-dimensional (Hills, 1974; Miyauchi and Shyu, 1970; Yang et al., 1986; Devanathan et al., 1990). These studies have provided much insight into the overall averaged flow field, which reveals the existence of the gross circulation flow field mentioned previously. Among the most useful data for model verification are those provided by Hills (1974), who used a pitot tube to measure the liquid velocity and voidage profiles. Attempts have also been made to study the instantaneous, microscopic flow phenomenon and relate this phenomenon to the overall or macroscopic behavior. Franz et al. (1984) used hot-film anemometry (HFA) to analyze the "instantaneous" axial, tangential, and radial velocities, and the turbulent intensity. They postulated a spiral upward macrovortex flow model consisting of three zones. This work provides important experimental evidence regarding the dynamic nature of the flow structure. More recently, Chen et al. (1994) studied the instantaneous behavior of bubble columns by using a nonintrusive particle image velocimetry (PIV) technique. Based on the instantaneous full-field flow results provided by the PIV technique, they quantified the flow characteristics underlying the instantaneous macroscopic flow structure. Chen et al. (1994) also showed that by averaging the instantaneous data from the PIV, they were able to obtain results (upward liquid flow in column center and downward liquid streams adjacent to the walls of the vessel) similar to those obtained by time-averaged techniques. It is clear that when the gross circulation occurs the instantaneous flow structures are different from those inferred by utilizing time/volume-averaging procedures.

Ulbrecht et al. (1985), by using viscous and non-Newtonian liquids, visualized three instantaneous flow patterns, and concluded that the flow structure and governing mechanisms depend on the column dimensions, gas distributor design, flow rate of the gas, and the physical properties of gas and liquid. Shah et al. (1982) pointed out that the most important "adjustable" parameter that can affect "non-adjustable parameters," namely, the phase holdup, gas–liquid interfacial area, and heat and mass transfer coefficients, is the diameter of the column. Chen et al. (1989) also found that if the aspect ratio of the liquid height to column diameter is over unity, the flow structure will change from "gulf circulation" to multiple circulation cells. Due to the limitation of the measuring techniques and the complicated mechanisms of the system, there is still a lack of detailed understanding of the hydrodynamics of bubble columns, such as the effects of scaling and gas velocity on the hydrodynamics (the gas holdup and liquid distribution in the bubble columns), the effects of gas and liquid properties on the scale-up, and the relationship between hydrodynamics and mass and heat transfer.

Two-dimensional (2-D) systems have been employed to yield important qualitative information in gas–liquid systems (Chen et al., 1989; Tzeng et al., 1993). Tzeng et al. (1993) used a 2-D column to investigate the macroscopic flow structures and mechanisms of liquid circulation. Based on the bubble dynamics and local liquid flow patterns, they found that when the gross flow circulation occurs in the system, there are four distinct flow regions, namely central plume region, fast bubble flow region, vortical flow region, and descending flow region, as shown in Figure 1a. Reese et al. (1993) and Chen et al. (1994) found through qualitative flow visualization that the flow structures in 2-D and three-dimensional (3-D) bubble columns are similar, as shown in Figure 1. The studies have indicated that similar flow regions exist in the 2-D and 3-D bubble columns. However, the wavelike motion of the fast bubble flow region in 2-D bubble columns becomes a spiral motion in 3-D bubble columns. This type of instantaneous flow phenomenon gives rise to time-averaged flow field of the liquid phase consisting of the previously discussed pair of gross circulating cells.

Computational studies

In order to obtain the time-averaged flow structure, the integral time length has to be much longer than the characteristic time length of the system. Therefore, when numerical simulations of these systems are based on time-averaged approaches, this special requirement of the integral time length will result in unrealistic prediction of the dynamic transport in actual bubble column systems. Many previous computational studies of the macroscopic behavior of bubbling flows have been associated with this time-averaged behavior in bubble columns. For instance, Geary and Rice (1992) used the separated-flow method to simulate the gas–liquid flow in a bubble column. The bubbling flow was assumed to be steady state, and any variations occur only in the radial direction. By neglecting end effects, typical time-averaged velocity and voidage profiles in the fully developed region were obtained. Svendsen et al. (1992) attempted to simulate bubbling flows in bubble columns using a two-fluid model. The turbulent effects were considered by employing the k-ϵ turbulent model. These time-averaged simulations all yielded a flow structure with a pair of overall circulating flows as discussed previously. Sokolichin et al. (1993) also used the two-fluid model to simulate the tiny bubble flow in a 2-D bubble column. In their study, Stokes' law was used to model the drag force between the bubble phase and the liquid phase. Lapin and Lübbert (1994) used both the two-fluid model and the bubble phase trajectory model to simulate tiny bubble flows in a 2-D column. They revealed that the Langrangian approach of the bubble phase can overcome the numerical diffusion effects on the gas phase computation encountered in the two-fluid model approach. Celik and Wang (1994) simulated the overall circulation flow pattern in bubble columns operated under the laminar, dispersed bubble regime. In their study, Celik and Wang (1994) used the two-fluid model with an empirically defined gas velocity field and a gas holdup profile that had an assumed shape or was calculated from the gas phase continuity equation. They used an empirical relation that only considers the viscous drag force of the gas phase to account for the momentum exchange between phases. Considering the discrete nature of the bubble phase, Webb et al. (1992) simulated the flow in a 2-D bubble column using the stochastic trajectory model to trace the movements of individual bubbles. The flow field of the liquid phase was determined by using the Eulerian approach. Their model yields a flow structure similar to that obtained from time-averaged approaches. Since the pair of circulating cells deviates significantly from the actual bubbling flow, time-averaged computations cannot provide a rational explanation of the transport processes of mass, momentum, and energy between the bub-

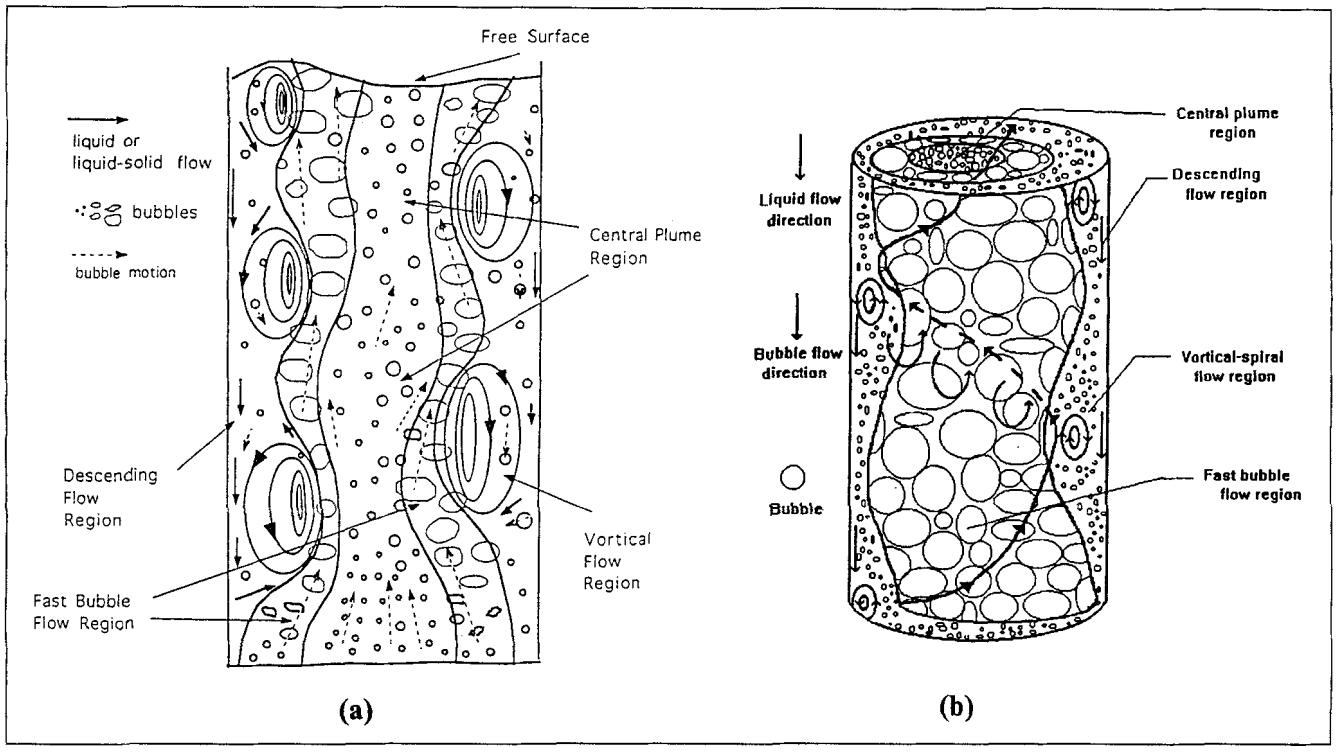

Figure 1. Classification of regions accounting for the macroscopic flow structures: (a) 2-D bubble column (Tzeng et al., 1993); (b) 3-D bubble column (Chen et al., 1994).

bles and liquid. Thus, a computation of the transient or instantaneous flow behavior is necessary.

This article studies the macroscopic hydrodynamic properties of 2-D bubble columns of varying width and gas velocity. These hydrodynamic properties are found to be related to the regime transition and the scale effects of 2-D bubble columns. A conceptual analogy of the wavelike motion is postulated based on the observations. In addition, the velocity distribution and gas holdup profiles are quantified by a PIV system to substantiate the macroscopic flow structure in various sizes of 2-D bubble columns. Numerical simulations of 2-D shallow beds are conducted under the dispersed bubble flow conditions to provide full field information including velocity and pressure distributions around the bubbles as well as their variations with respect to time. The transient numerical results are investigated and discussed in relation to the experimentally observed macroscopic hydrodynamic properties.

Experimental Apparatus

Figure 2 shows the experimental system. Three 2-D columns made of transparent Plexiglas sheets are used as the test columns. Column A is 48.3 cm in width, 1.27 cm in depth, and 160 cm in height and consists of two movable partitions between the Plexiglas sheets that allow the width of the bed to be varied. The viewing section of column B is 60.96 cm in width, 228.6 cm in height, and 0.64 cm in depth. Table 1 summarizes the dimensions for these two columns. Below the viewing section is the gas distributor, which consists of 0.016-cm-ID tube injectors, flush mounted on the column wall, 10 cm above the liquid inlet. The gas flow through each injector is individually regulated by a solenoid valve and a needle valve that are connected to the plenum compartment outside the bed. The distance between two adjacent bubble injectors is 5.08 cm and the distance from the end injector to the sidewall is 3.81 cm. When the width of column A is changed, there is no liquid and gas flow through the region outside the partitions. Column C is a small column, 24 cm in width, 0.635 cm in depth, and 30 cm in height and also consists of two movable partitions between the Plexiglas sheets. The column can be operated with two- or three-bubble injectors. Figure 3 demonstrates the experimental dimensions of column C.

For columns A and B, tap water is used as the liquid phase. The liquid phase is operated under batch conditions for all studies. Neutrally buoyant Pliolite particles of 200–500 μm are used as the liquid tracer. To ensure that the seeding particles follow the flow closely and have virtually no effects on the flow structure, the concentration of the seeding particles is maintained around 0.1% and the Stokes number of the seeding particles is much smaller than 1. Air is used as the gas phase. The gas pressure is maintained within 4 to 10 psig (128–170 kPa) upstream of the gas plenum. The superficial gas velocity ranges from 0.1 to 6.1 cm/s. Acetate particles ($d_p = 0.15$ cm, $\rho_s = 1.25$ g/cm^3) are used as the solids phase in the study of gas–liquid–solid fluidization systems. Column C is operated under gas–liquid conditions. Both water and 80% glycerine solution are used as the liquid phase. In the following discussion, results from columns A and B are presented, as well as the results from column C, which are discussed in conjunction with the computational fluid dynamic

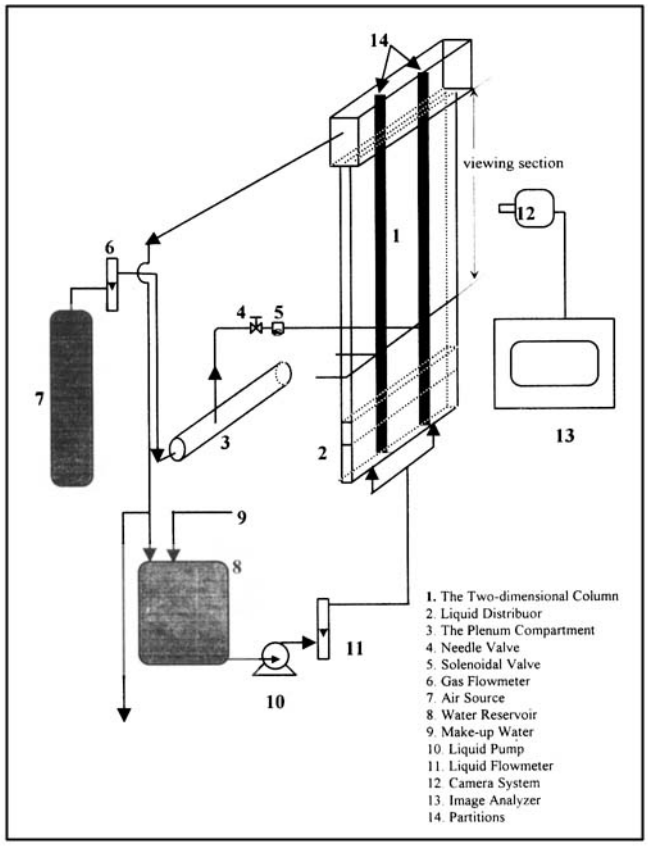

Figure 2. Two-dimensional fluidized bed.

1. The 2-D column; 2. liquid distributor; 3. the plenum compartment; 4. needle valve; 5. solenoidal valve; 6. gas flowmeter; 7. air source; 8. water reservoir; 9. make-up water; 10. liquid pump; 11. liquid flowmeter; 12. camera system; 13. image analyzer; 14. partitions.

work. All the gas velocities described in the text refer to the superficial velocities unless otherwise stated.

A high-resolution (800×490 pixel) CCD camera equipped with variable electronic shutter ranging from 1/60 to 1/8,000 s is used to record the image of the flow field. A PIV system developed by Chen and Fan (1992) is applied to measure local flow structures in the 2-D bubble columns. The PIV system is a nonintrusive technique that provides quantitative results on a flow plane including instantaneous velocity distributions of different phases, velocity fluctuations, accelerations, gas and solid holdups, bubble sizes and their distributions, and other statistical flow information.

Table 1. Dimensions of the Test Columns

Column	Width	Height of Viewing Section	Depth	Total Height of Bed
A	10.16	160	1.27	240
	15.24	160	1.27	240
	20.32	160	1.27	240
	30.48	160	1.27	240
	48.26	160	1.27	240
B	60.96	229	0.64	300

Note: Unit = cm.

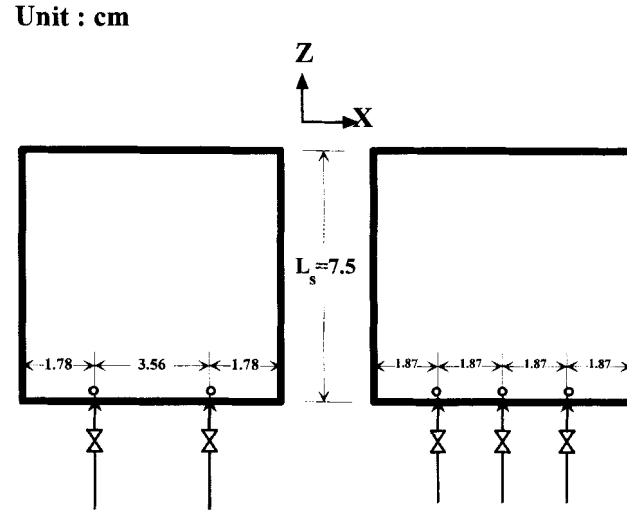

Figure 3. Dimensions of the 2-D bubble column for two- and three-bubble injector setups.

Results and Discussion

Quantitative analysis (experimental)

Macroscopic Flow Structure. Figure 4 shows a sample of the bubbling behavior in the dispersed bubble regime and coalesced bubble regime including 4-region flow and 3-region flow in a 2-D bubble column. This bubbling behavior corresponds to flow conditions of increasing gas velocity. The dispersed bubble flow regime exists up to a gas velocity of 1 cm/s. This regime is characterized by a relatively uniform gas holdup profile, uniform bubble size, and a rather flat liquid velocity profile. The bubbles in this regime are observed to rise rectilinearly in the form of bubble streams. No coalescence or clustering of the bubbles in the individual bubble streams or with adjacent bubble streams occurs. The liquid phase is carried upward in the region of the bubble streams by the wake motion and the liquid drift effects associated with the bubble motion. The liquid falls downward between adjacent bubble streams with continuous downward streams adjacent to the sidewalls. This descending motion of the liquid coupled with the rising motion of the adjacent bubble stream generates small vortices in the liquid streams between the rising bubble streams and the region adjacent to the sidewalls. The vortices located adjacent to the sidewalls are observed to increase in size as the gas velocity increases in the dispersed bubble regime due to the migration of bubbles away from the sidewalls. In this regime, the induced liquid flow is dominated by the drift effects of the rising bubble streams.

The 4-region flow condition exists for gas velocities between 1 and 3 cm/s. This condition is characterized by a gross circulation of the liquid phase, wherein the liquid rises in the middle portion of the column and descends adjacent to the sidewalls. The four flow regions (Figure 1a) and the resulting flow phenomena were reported by Tzeng et al. (1993). In columns of width less than 20 cm the central plume region

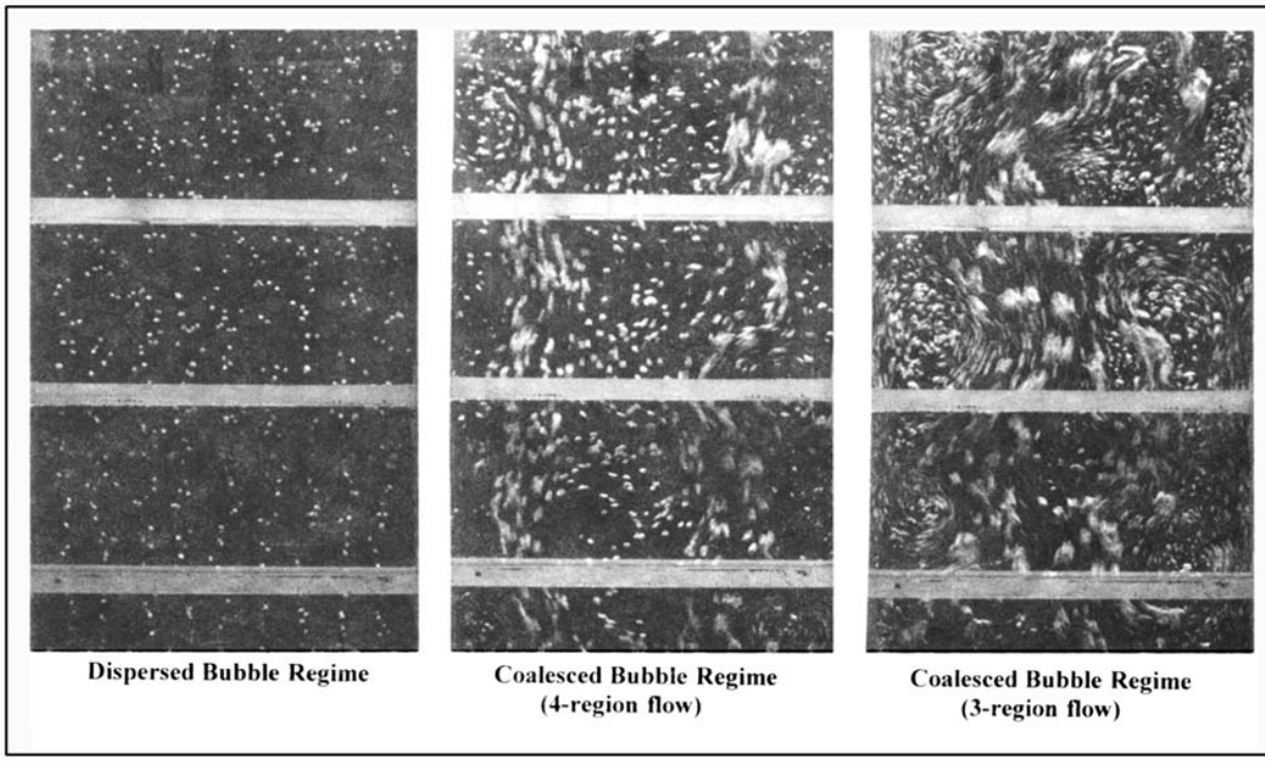

Figure 4. Flow regimes in a two-dimensional bubble column.

becomes indistinguishable from the fast bubble flow region yielding a 3-region flow.

The 3-region flow condition occurs at gas velocities greater than 1 cm/s for small columns (< 20 cm width) and at 3 cm/s for larger columns (> 20 cm). In the 3-region flow condition the two fast bubble flow regions merge together to form one central fast bubble region in the center of the column. The gas flow in this regime is dominated by bubble coalescence and breakup. The liquid flow is dominated by the wake effects from the large bubbles rising in the central part of the column. The vortical flow region and descending flow regions are still observable. It is noted that in a column of very small width, this flow commonly leads to the slugging condition.

Wavy Phenomena. In a previous study, Tzeng et al. (1993) found that when the gross circulation of the liquid phase occurs, the migration of the bubbles away from the sidewalls causes bubble coalescence and the creation of the fast bubble flow region which strengthens the vortical flow and the descending flow regions. The vortical flow region consists of multiple vortices located along the sidewalls in the axial direction. For a large column, the vortices on either side of the column exist independent of each other at low to moderate gas velocities. However, at high gas velocity the vortices become staggered similar to those in a small column. The interaction between the vortical flow region and the fast bubble flow region leads to the existence of crests (when vortices are present) and troughs (in the absence of vortices) in the fast bubble flow region. Therefore, the fast bubble flow region moves in a wavelike manner and can be said to follow a wave motion similar to a string.

Figure 5 shows the definition of vortex size and wavelength considered in this study. From flow visualization, the boundary of a vortex can be identified by the outermost closed loop of tracer trajectories and the size of a vortical circulation is herein defined as the lateral length of this boundary. In Figure 5, it can be seen that the vortex size is approximately equal to twice the amplitude of the wave. The wavelength is defined as the distance between two crest (or trough) points of the outermost closed loop of the tracer trajectories.

Figure 6 shows the variation of the vortex size with respect to the gas velocity in 2-D columns of different width. From the figure, it can be seen that, independent of the column width, the vortex size increases with gas velocity up to 1 cm/s, beyond which the vortex size remains constant. Figure 6 implies that when the gas velocity is about 1 cm/s, the bubbles near the sidewalls start to migrate at the onset of gross circulation and generate the multivortices to form the vortical flow region. At this gas velocity, the bubbles move in clusters and no bubble coalescence is observed. As the gas velocity increases beyond the transition velocity, 1 cm/s, bubble coalescence and breakup take place to form the fast bubble flow region. This fast bubble flow region will strengthen the vortical flow, but confine the growth of the vortex size between the sidewalls and the concavity of the fast-moving coalesced-bubble streams. This fast bubble flow region, which acts as a barrier for the radial mass transfer for both the solids and the liquid phase, is observed for both 2-D and 3-D columns (Chen et al., 1994). As mentioned, the vortex size remains constant for gas velocities above 1 cm/s, therefore, the fast bubble flow region grows inward, swinging in a wavelike manner while the central plume region progressively diminishes. Figure 6 also shows that the maximum vortex size increases as the column width increases. However, when comparing the ratio of vortex size to column width in columns of varying

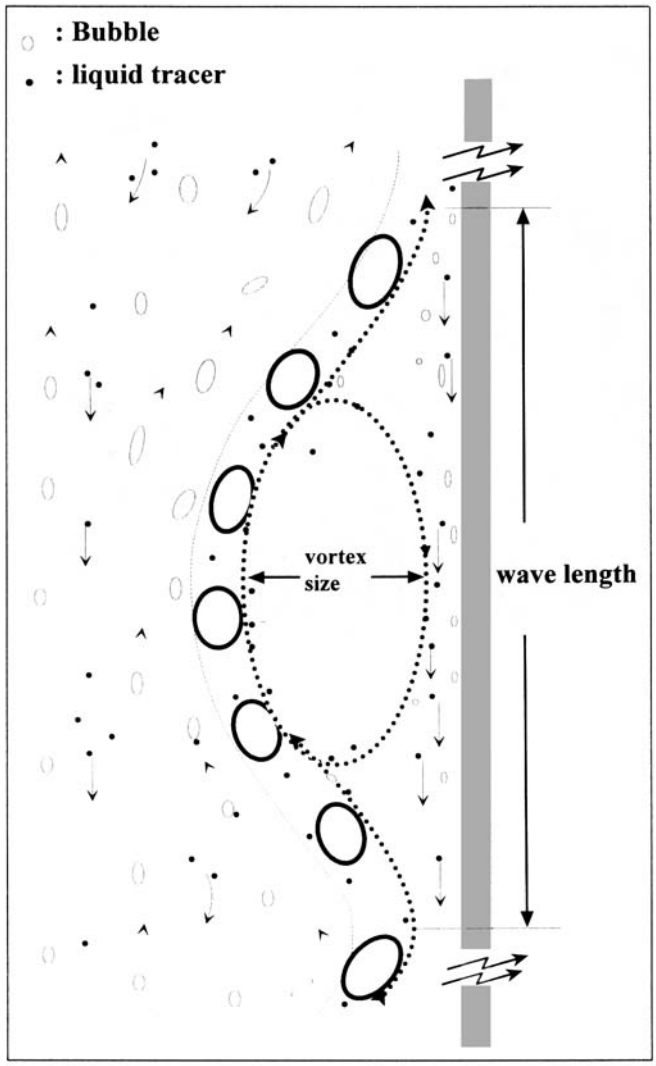

Figure 5. Definition of vortex size and wavelength.

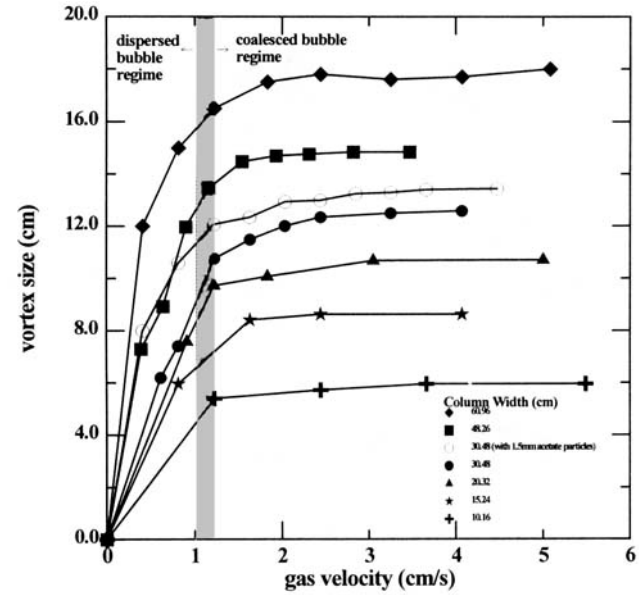

Figure 6. Variation of vortex size with gas velocity in columns of different width.

width (Figure 7), it is seen that the ratio in a smaller column is larger than that in a larger column. This indicates that as the column width increases, the outer shell, including the vortical flow and the descending flow regions, occupies a smaller portion of the column than the inner part, including the fast bubble flow and central plume regions.

In Figure 8, the wavelength of the fast bubble flow region decreases with gas velocity up to 3 cm/s, beyond which it remains relatively constant. When the gas velocity increases to around 3 cm/s, the two fast bubble flow regions merge together to form one central bubble stream that moves in a wavelike manner and the central plume region disappears. The new central bubble stream has a constant wavelength as the gas velocity increases. From Figure 8 it is also found that the wavelength in a small column is less than that in a large column at the same gas velocity.

The multiple vortex cells that are continually generated in the vortical flow region become confined by the wave motion of the fast bubble flow region. The behavior of these vortices is dynamic in nature and the formation of these vortices at each sidewall appears to be independent of each other. That is, the entire vortex flow region is swinging laterally back and forth corresponding to the wave motion of the neighboring fast bubble flow region. Therefore, the frequency of the wave motion can be obtained by counting the number of vortices that pass a specific location near the sidewall. Figure 9 shows the variation of frequency with gas velocity in columns of different width. The frequency increases with the gas velocity in any 2-D bubble column. This is because at high gas velocities, bubbles coalesce to form larger bubbles, which impart higher kinetic energy to the liquid phase and thus, increase the fre-

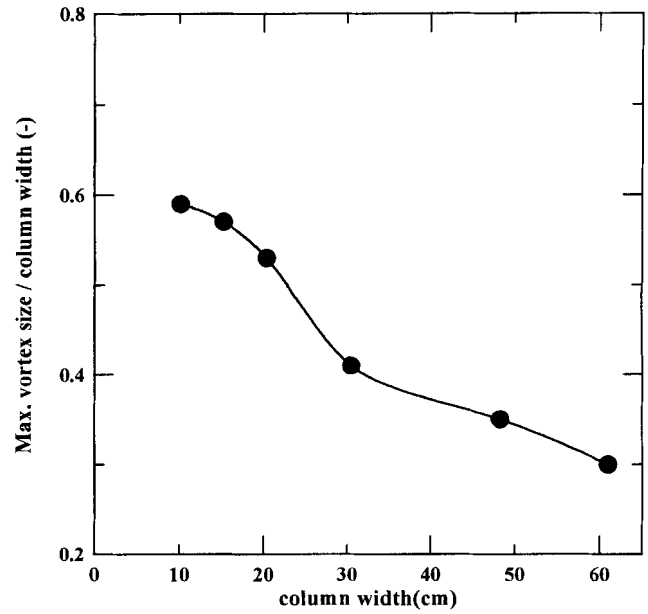

Figure 7. Ratio of maximum vortex size to column width vs. column width.

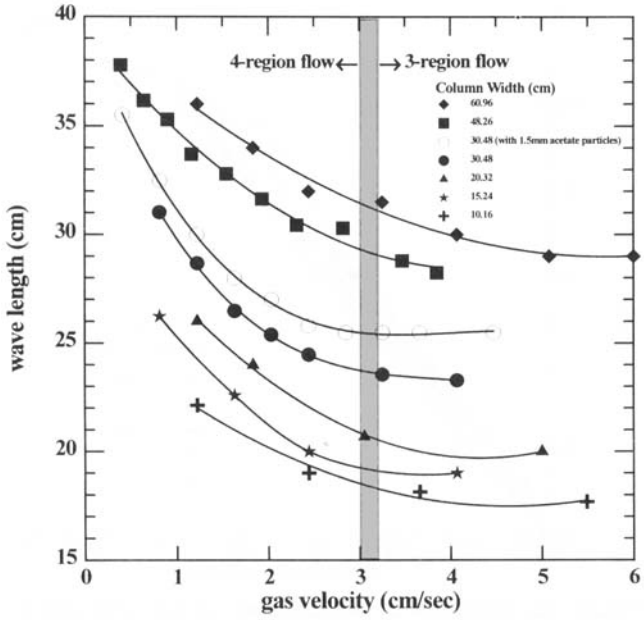

Figure 8. Variation of wavelength with gas velocity in columns of different width.

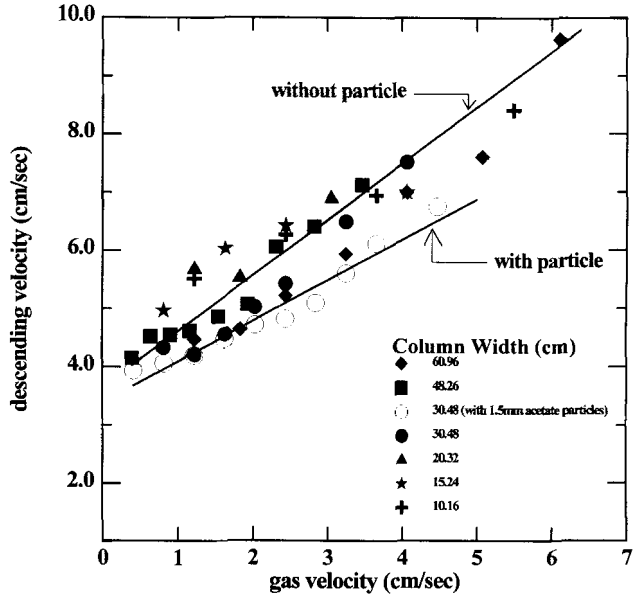

Figure 10. Variation of vortex descending velocity with gas velocity in columns of different width.

quency of the wave motion. Higher frequency also occurs in smaller bubble columns at the same gas velocity.

Since the fast bubble flow region moves in a wavelike manner, the rising velocity of the fast bubble flow region, and thus the vortex descending velocity, can be accounted for by the wave velocity. As described, the vortices stagger with the fast bubble flow region and descend along the sidewall. From wave theory, the wave velocity, which defines the vortex descending velocity, is equal to the generation frequency times the wavelength, given by

$$V_D = W * f, \tag{1}$$

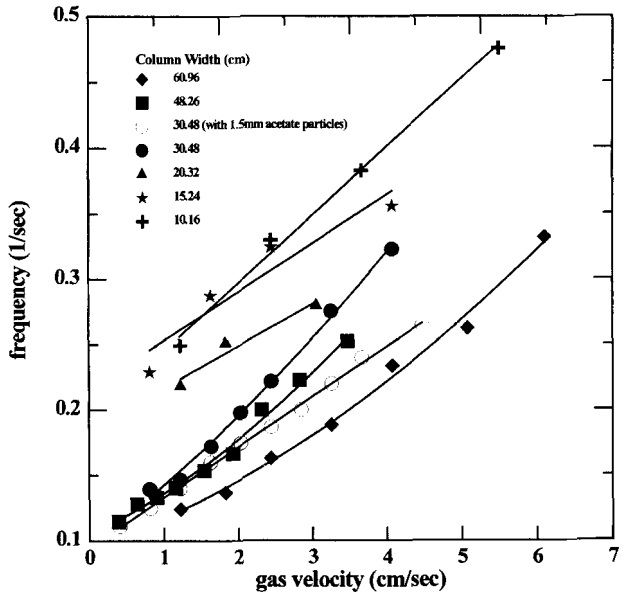

Figure 9. Variation of frequency with gas velocity in columns of different width.

where V_D, W, and f are vortex descending velocity, wavelength, and frequency, respectively. Figure 10 shows the variations of vortex descending velocity with gas velocity in columns of varying width. The figure indicates that the vortex descending velocity is determined by the gas velocity rather than the width of the column. This trend may provide a qualitative link to the 3-D scale effect.

Particle Effects. In studying the particle effects on a 2-D gas–liquid–solid fluidization system Tzeng et al. (1993) found that at solids holdup less than 20%, the general macroscopic flow structure for these systems is well represented by that for bubble column systems. In the present study, 1.5-mm acetate particles are used to elucidate the particle effects at low solids holdup ($< 10\%$) on the various wave-related phenomena discussed earlier. In Figures 6, 8, 9 and 10 the particle effects in a 30.48-cm column on the vortex size, wavelength, frequency, and vortex descending velocity are shown. As seen from the figures, the system operated with particles demonstrates similar trends as the bubble column systems. However, the quantitative results differ due to a change in the rheological properties of the mixture attributed to an increase in the apparent viscosity of the mixture when the solid phase is present. In this system with low-density particles, an increase in the apparent viscosity leads to a larger bubble size, and thus an increase in the rate of bubble coalescence. An increase in the rate of bubble coalescence affects the demarcation of the flow condition in a three-phase system. From Figure 8, it can be seen that the wavelength levels off quicker in the presence of a solid phase, indicating that the transition from 4-region flow to 3-region flow occurs at a lower gas velocity.

Figure 10 shows that the descending vortex velocity of the three-phase system deviates from the gas–liquid systems especially at high gas velocity. This deviation can be further understood by considering the frequency in Figure 9. The decreased rate of increasing frequency shown in Figure 9 for the three-phase system directly affects the vortex descending

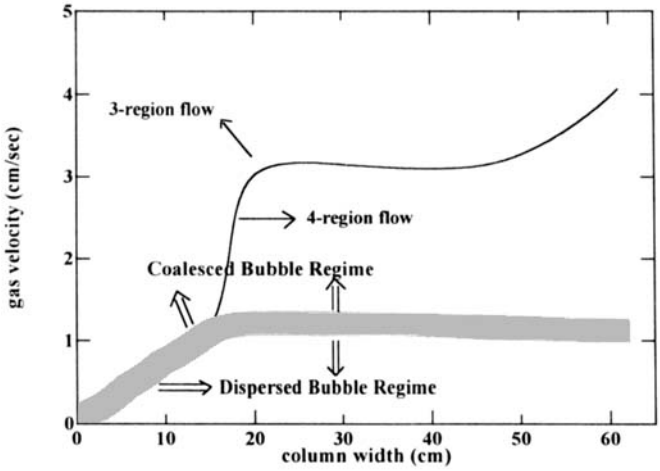

Figure 11. Operating regimes of 2-D bubble columns.

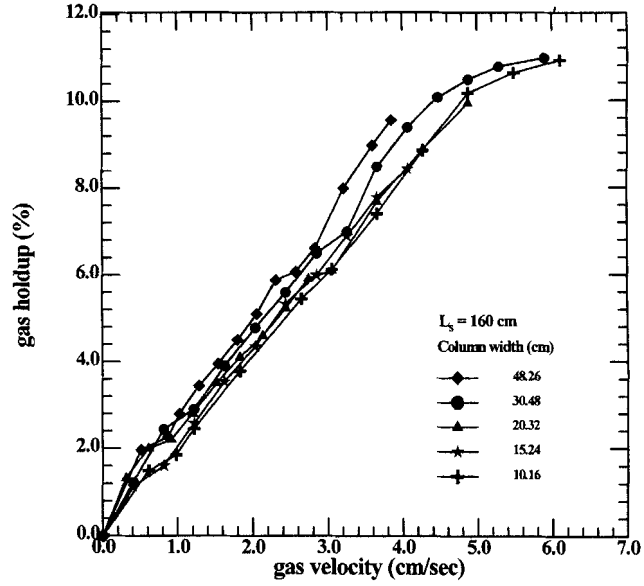

Figure 12. Variation of overall gas holdup with gas velocity in columns of varying width.

velocity. The results demonstrate that, although the parameters associated with the wave-related phenomena are affected by the presence of a solid phase, the general macroscopic behavior of a 2-D gas–liquid–solid fluidization system at low solids holdup is similar to that for a bubble column system.

Scale Effects. Based on flow visualization and the description of the flow regimes given earlier, the approximate dependency of the flow regimes on gas velocity and column width can be determined. Figure 11 shows that in columns less than 20 cm in width, by increasing the gas velocity, the flow regime will change directly from the dispersed bubble flow regime to 3-region flow. However, in larger columns, the flow regime will change from dispersed bubble flow, to 4-region flow, and then to 3-region flow. In large columns when the gas velocity reaches 1 cm/s the vortex size does not increase. Therefore, by continuously increasing the gas velocity the fast bubble flow regions will gradually grow and merge to form a central fast bubble region in which the bubbles coalesce and break up violently. However, in small columns, the bubbles merge together quickly to form a central bubble flow region that occupies the central plume region directly. Figure 11 shows that 1 cm/s and 3 cm/s are the demarcations between the dispersed bubble flow regime to the 4-region flow, and 4- to 3-region flow, respectively. Figure 11 is compared with the regime classification for 3-D systems reported by Shah et al. (1982), the two figures (Figure 11 and Figure 2.2 of Shah et al., 1982) bear considerable resemblance for dispersed bubble regime and coalesced bubble regime. Thus, it is apparent that the 2-D column results obtained in this study reveal that the coalesced bubble regime (or churn-turbulent flow) can be subdivided into 4-region flow and 3-region flow.

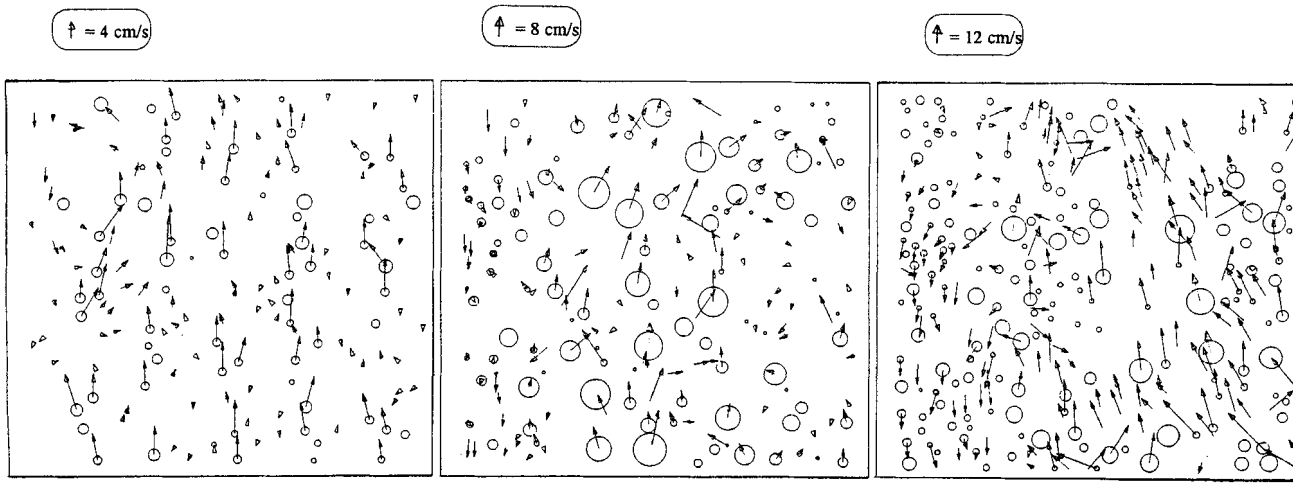

Dispersed Bubble Regime | **Coalesced Bubble Regime (4-region flow)** | **Coalesced Bubble Regime (3-region flow)**

Figure 13. Instantaneous velocity vectors of liquid and gas (shown with bubble size) at L_m = 80 cm for left half of a 48.3-cm column for gas velocities of 0.26, 1.54 and 3.34 cm/s.

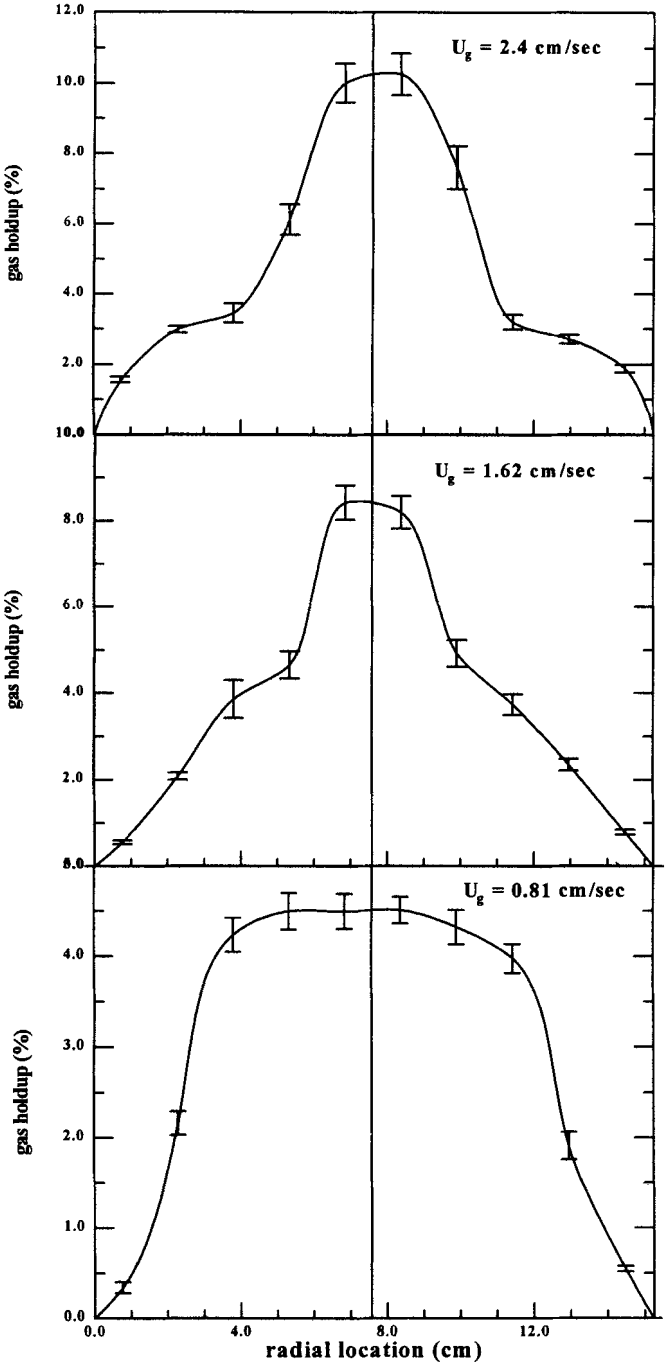

Figure 14. Radial gas holdup distribution in 15.24-cm column for $L_m/L_s = 0.5$ and $U_g = 0.81$, 1.63, 2.4 cm/s.

In a 3-D system the flow will change from the dispersed bubble flow regime at lower gas velocities, to the coalesced bubble regime that has been found to consist of the vortical spiral and turbulent flow conditions at high gas velocities (Chen et al., 1994). Here, the 3-region flow in a 2-D system, which exhibits coherent flow structures, will transform to the turbulent flow condition in the 3-D system when the gas velocity continues to increase. Even though the flow field in a 2-D column deviates to some extent from that in a 3-D column, the present results provide the qualitative and quantitative similarities of dynamic flow structure between 2-D and 3-D bubble columns.

Overall Gas Holdup. The overall gas holdup of a bubble column is defined by

$$\epsilon_{av} = (L_f - L_s)/L_f, \tag{2}$$

where L_f and L_s are the bubbling bed height and the static liquid height, respectively. Measured values of ϵ_{av} in columns of varying width are shown in Figure 12. The figure indicates that ϵ_{av} does not strongly depend on the column width. However, it can be seen that the slope of the curves change at gas velocities around 1 cm/s and 3 cm/s. The first change marks the onset of the coalescence of bubbles near the sidewall to form the two fast bubble flow regions in large columns (or one central fast bubble flow region in smaller columns) that occurs at a gas velocity around 1 cm/s. Thus, the bubble size increases, which reduces the rate of the increase of ϵ_{av}. When the gas velocity increases to 3 cm/s in large columns, ϵ_{av} undergoes another prominent change, which is caused by the two fast bubble flow regions merging together to form one central fast bubble flow region. Therefore, the rate at which ϵ_{av} increases will again decrease. The phenomena of changing ϵ_{av} corresponding to column width and gas velocity match the division of operating regimes as shown in Figure 11. Although ϵ_{av} measured in 2-D columns is different from that in 3-D columns, the results yield important qualitative and quantitative relevance of scale effects on gas holdup.

Local Gas Holdup and Liquid Velocity Behavior. The PIV technique employed in this study is capable of providing the instantaneous gas holdup and liquid velocity profiles at any location in the column without disturbing the flow. Figure 13 shows representative examples of the instantaneous flow phenomena occurring in the dispersed bubble regime, and the coalesced bubble regime (4-region flow and 3-region flow) for the left half of a 48.3-cm column. The figure illustrates the instantaneous velocity vectors of the liquid and gas phases (shown with the bubble size) over a time interval of 1/30 s. These instantaneous data can be time and volume averaged to yield the averaged gas holdup and liquid velocity distributions in the system.

As previously mentioned, the flow regime transition, and subsequently the gas holdup distribution, in small columns differs from that in large columns. In small columns, the bubbles coalesce at the bottom of the column right above the bubble injectors, and therefore the flow structure develops quickly in the axial direction. Thus, the gas holdup distribution remains constant through the entire region above the injector. Figure 14 shows the effect of the gas velocity on the radial distribution of the gas holdup measured at $L_m = 80$ cm ($L_m/L_s = 0.5$, where L_m is the height above the bubble injectors) in a 15.24-cm-wide bubble column. The figure illustrates that the shape of the radial gas holdup distribution shifts from a uniform bubbly distribution at low gas velocity to a central bubble distribution at higher gas velocities. This result asserts that in small columns the flow regime transforms directly from the dispersed bubble flow regime to the 3-region flow condition.

In large columns, as noted, the flow structure changes with gas velocities from the dispersed bubble flow to 4-region flow, and from 4-region flow to 3-region flow. Figure 15 shows the

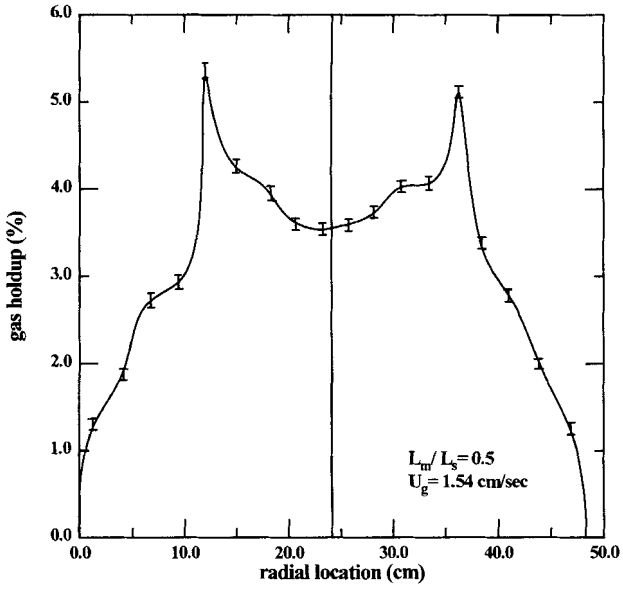

Figure 15. Radial gas holdup distribution in 48.3-cm column, demonstrating that the holdup behavior in the column is symmetric.

radial gas holdup distribution in the entire 48.3-cm column for a gas velocity of 1.54 cm/s; the figure reveals the radial symmetric behavior of the gas holdup.

At a low gas velocity, the bubble streams are observed to rise rectilinearly with relatively uniform size distribution along the column radius and axis. Thus, in the dispersed bubble regime, the radial and axial gas holdup distributions are uniform, except near the sidewalls, as shown in Figure 16a for a 48.3-cm column. A typical radial liquid velocity profile in this dispersed bubble regime is shown in Figure 16b. The liquid is carried up by the bubble-driven motion in the vicinity of the ascending bubble streams. Although some liquid flows downward between these bubble streams, the averaged liquid velocity is upward in this region. The liquid is seen to descend in the region near the sidewalls.

When the gas velocity is increased to 1 cm/s, bubble clustering or coalescence occurs that is induced by the migration of bubble chains near the sidewalls and by the presence of the growing vortices near the gas distributor in the vortical flow region. The coalesced or clustered bubbles form the fast bubble flow region that has the highest gas holdup in the radial distribution, as shown in Figure 17a. Figure 17b shows the time and volume averaged axial liquid velocity profiles at different axial locations in the 48.3-cm column for a gas velocity of 1.54 cm/s. This figure shows that the axial liquid velocity, induced by the bubble wake and bubble carriage motion, moves uniformly upward in central plume region. The upward velocity increases to a maximum when the liquid is carried upward by the large bubbles in the fast bubble flow region. Then, the upward velocity decreases sharply with radial direction and becomes zero at the location between 60% and 70% of the column half width. After the inversion point, the downward velocity increases with the radial distance to the location at 90%. The results are similar to the 3-D reported previously (Hills, 1974). In addition to moving upward in the axial direction, the fast bubbles grow and migrate laterally toward the center of the column. This is due to the gradual increase in bubble size in the axial direction, with the vortex size remaining constant. Therefore, the central plume region decreases near the top of the column. Figures 17a and 17b show this behavior in the upper part of the column. The PIV results again reveal that the gross circulation flow pattern includes the upward flow in the column center and downward flow in column wall.

Increasing the gas velocity yields the 3-region flow condition. In the region immediately above the gas injector, the radial gas holdup is uniform, as shown in Figure 18a. However, the large bubbles coalesce and form a central fast bubble flow region that yields a gas holdup in the center higher than that in the other regions. There is no central plume region in the 3-region flow condition. Due to the interaction

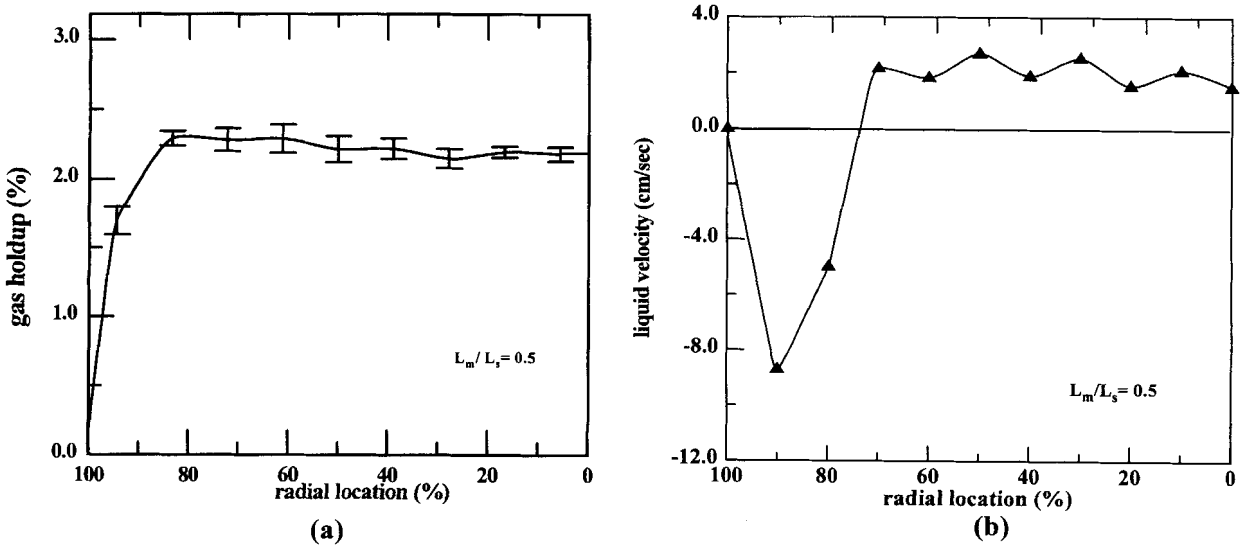

Figure 16. Radial gas holdup (a) and axial liquid velocity (b) distribution in 48.3-cm column at low gas velocity ($U_g = 0.26$ cm/s).

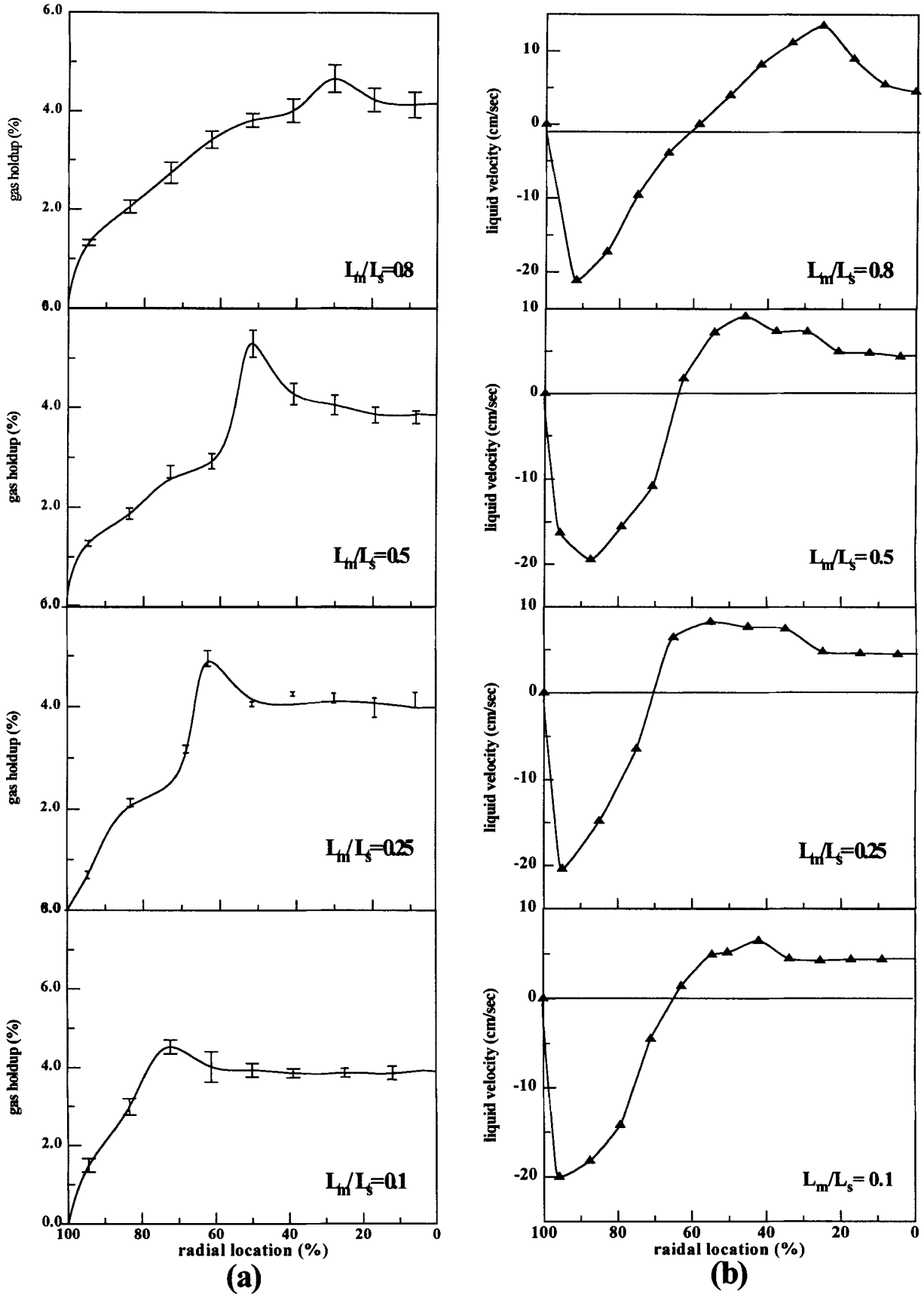

Figure 17. Radial gas holdup (a) and axial liquid velocity (b) distribution in 48.3-cm column at various axial locations and $U_g = 1.54$ cm/s.

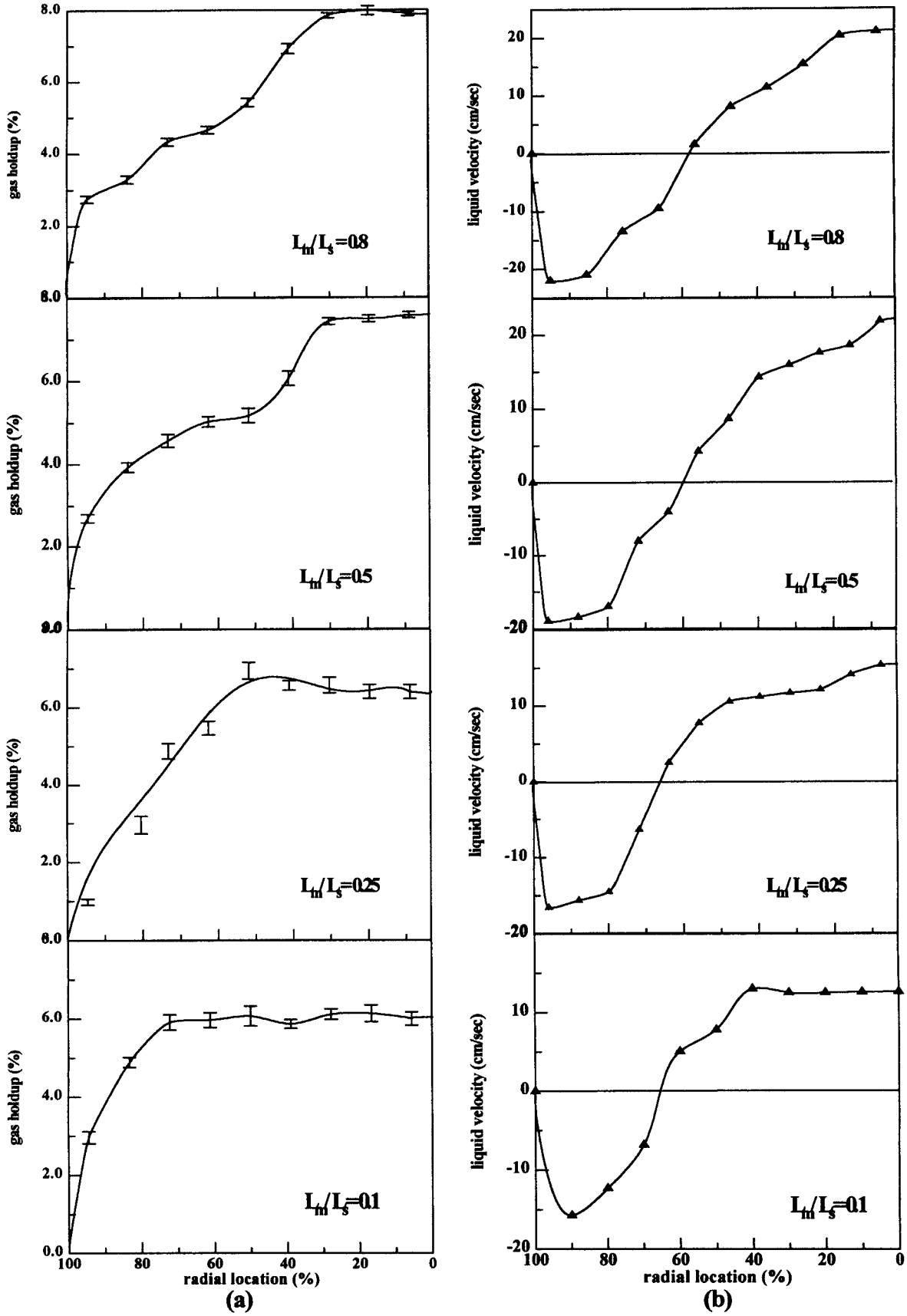

Figure 18. Radial gas holdup (a) and axial liquid velocity (b) distribution in 48.3-cm column at various axial locations and $U_g = 3.34$ cm/s.

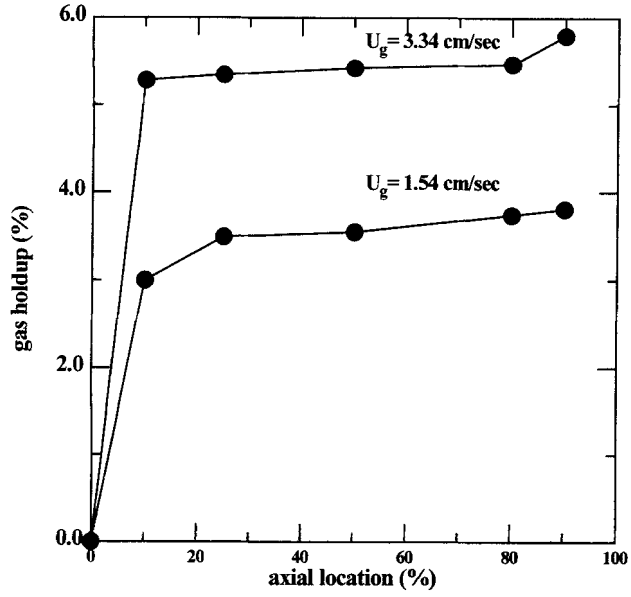

Figure 19. Axial gas holdup distribution in 48.3-cm column for U_g = 1.54 cm/s and 3.34 cm/s.

between the vortices and fast bubble flow region, small bubbles are trapped into the vortical and descending flow regions. Thus, the gas holdup near the sidewalls at high gas velocities is higher than that at lower gas velocities. Figure 18b presents the axial liquid velocity profile in the radial direction at different axial locations. The figure shows that the maximum axial liquid velocity is in the central region that differs from that in the 4-region flow condition, as the bubbles coalesce immediately above the distributor region. As a consequence of the larger wake effects generated by larger bubbles in this flow, the maximum axial liquid velocity in 3-region flow is greater than that in 4-region flow. The position of the inversion point is almost the same as that in 4-region flow. This is due to the vortex size remaining constant when the gas velocity is over 1 cm/s. Due to the increased bubble wake effects, the mass flux of the liquid in the vortical and descending flow regions is greater than that in the 4-region flow condition.

The cross-sectional average axial gas holdup distributions in the 48.3-cm column operated in the 4- and 3-region flow conditions are also measured, as shown in Figure 19. This figure shows that the flow at high gas velocity develops more rapidly than at low gas velocity. This is reflected by the constant value of the gas holdup observed throughout most of the column at high gas velocity. In this study, data obtained on the wavelength, vortex size, and holdup are typical for the bulk region of the bed.

Computation

Numerical technique

Liquid Phase Motion. In this study, the 2-D behavior of a gas–liquid flow in a bubble column is simulated. The differential equations are expressed in Cartesian coordinates (x, z). The motion of the liquid phase is simulated by solving the instantaneous Navier–Stokes equations with appropriate boundary conditions. The liquid phase is assumed to be incompressible, giving the mass conservation equation as

$$\frac{\partial u}{\partial x}+\frac{\partial w}{\partial z}=0, \tag{3}$$

where u and w are the liquid phase velocities in the x and z directions, respectively. The liquid phase momentum equations are expressed by

$$\frac{\partial u}{\partial t}+u\frac{\partial u}{\partial x}+w\frac{\partial u}{\partial z}=-\frac{1}{\rho}\frac{\partial p}{\partial x}+\frac{\mu}{\rho}\left[\frac{\partial^2 u}{\partial x^2}+\frac{\partial^2 u}{\partial z^2}\right] \tag{4}$$

$$\frac{\partial w}{\partial t}+u\frac{\partial w}{\partial x}+w\frac{\partial w}{\partial z}=-\frac{1}{\rho}\frac{\partial p}{\partial z}-g+\frac{\mu}{\rho}\left[\frac{\partial^2 w}{\partial x^2}+\frac{\partial^2 w}{\partial z^2}\right], \tag{5}$$

where ρ is the density of the liquid, p is the liquid phase pressure, μ is the viscosity of the liquid, and g is the gravitational acceleration. Equations 3, 4, and 5 are solved to provide the liquid phase velocity field and the liquid phase pressure distribution.

Bubble Motion (Gas-Liquid Interface). Across a gas–liquid interface, the physical properties change drastically from one phase to the other. The simulation of such an interface in multiphase flows has been a challenging problem since the beginning of large-scale computational studies. So far, two simulation approaches, the front-capturing method and the front-tracking method, have been developed to deal with this type of interface. The basic idea of the front-capturing approach is to discretize the whole computational domain in terms of the finite volume method, and at the same time, to use a higher order scheme and artificial viscosity around the interface to prevent the numerical solution from oscillating. Although well applicable for shock fronts, the front-capturing methods generally do not work as well for material interfaces (Boris, 1989). Other major drawbacks of this method include the requirement of relatively fine grids as well as associated technique complexities. The front-tracking method, meanwhile, considerably reduces the requirement of resolution to keep the front sharp and effectively eliminates the numerical diffusion. The volume of fluid (VOF) technique (Hirt and Nichols, 1981) is one of the front-tracking methods. The VOF method provides a simple and economical way to track the gas–liquid interface with reasonable accuracy and minimum storage requirements.

The VOF method is used in this study to track the sharp front between the bubble and liquid. The treatment of the gas phase in the VOF method differs from trajectory models or multifluid models in that each bubble is simulated by tracking the movement of its surface, that is, the gas–liquid interface. In order to maintain adequate resolution, the grid system has to be fine enough to provide a sufficient number of cells to represent a bubble as well as its surface. The motion, shape, volume, and inside pressure of a bubble are determined by the motion of the bubble surface. Unlike other methods, in the VOF method there is no assumption about the gas–liquid momentum transfer, and the gas–liquid interactions are directly determined by the simulated motion of the gas–liquid interface. Therefore, the factors affecting the gas–liquid interaction (i.e., surface tension effect, pressure distribution, and local liquid velocity fields) can be directly investigated.

The movement of a gas–liquid interface is tracked based

on the distribution of function, F, defined as the volume fraction occupied by the liquid phase in a computational cell. In the pure liquid region, F is equal to one and inside a bubble, F is equal to zero. The gas–liquid interface exists in cells where F lies between 0 and 1. Therefore, if the distribution of F is known at every moment, the location and shape of the bubbles are known. Due to the mass conservation of the liquid phase, the time-dependent governing equation of F is

$$\frac{\partial F}{\partial t} = -u\frac{\partial F}{\partial x} - w\frac{\partial F}{\partial z}. \tag{6}$$

At each time step, after the velocity field of the liquid phase is computed, Eq. 6 is used to update the F distribution, so that the location and shape of the bubbles at each time step can be obtained.

The present computational scheme ignores the transfer effects of the motion of gas inside the bubble on the interfacial gas–liquid momentum and thus the applicability of the scheme is limited only to gas bubble flow situations involving low pressure or low gas density conditions. The deformation of a bubble is assumed to be isentropic so that the pressure inside the bubble, p_g, can be related to its volume, v, by

$$p_g v^{\gamma} = \text{constant}, \tag{7}$$

where γ is the ratio of the specific heats.

Using the bubble shape determined by the F distribution, the surface curvature at any point along the bubble surface can be determined. The surface tension of the liquid together with the surface curvation determines the pressure difference across the bubble surface, Δp, from the Laplace–Young equation

$$\Delta p = \frac{2\sigma}{R}, \tag{8}$$

where σ is the surface tension of the liquid and R is the radius of surface curvature. By adding the pressure difference across the bubble surface (Δp) and the pressure inside the bubble (p_g), the pressure distribution along the bubble surface on the liquid side can be determined. This liquid phase pressure distribution adjacent to the bubble is used as a boundary condition while solving the momentum equation of the liquid phase adjacent to the bubble. The liquid flow field is then used to recalculate the F distribution, the bubble volume, the internal pressure, and the bubble shape. In this way, the momentum transfer between a bubble and its surrounding liquid is implicitly simulated. It is assumed that on the bubble surface there is no friction drag, which is reasonable since the gas motion inside the bubble is ignored and the gas phase viscosity is several orders or magnitudes lower than that of water.

In the simulation, the nonslip condition is used on the two sidewalls and the bottom of the column. On the top of the column the free boundary condition is used, except that, for simplicity, the axial liquid velocity (w) at the top boundary is assumed to be zero. The bubbles introduced are spherical in shape near the bottom of the column, and they leave the column when they reach the top of the computational domain. Initially, the liquid phase inside the column is in a static state. The simulation considers only the dispersed bubble flow.

In this study, the finite difference method is used for the numerical solution. The solution algorithm of Harper et al. (1991), which is based on the MAC method (Harlow and Welch, 1965), used in the well-known SOLA code (Hirt et al., 1975) is adopted in this study. It is noted that in this kind of solution algorithm, the numerical stability requires very short time steps, and a large amount of computational time is needed. The simulation is conducted on a CRAY Y-MP8/864 supercomputer at the Ohio Supercomputer Center.

Computational results

Due to grid limitations, only a shallow bed ($L_s/D \approx 1$) portrayed by column C (see Figure 3 for experimental arrangements) is simulated in this study. The grid system is set up to provide 98 grids in the z (vertical) direction and 93 grids in the x (horizontal) direction for the two-bubble injector case, while for the three-bubble injector case 98 grids are used in both the x and z directions. In these computations, no bubble collisions are considered. The computation of the 2-D geometry is conducted by considering the third dimension to be infinite. In the computation, two- and three-bubble injectors are set up in air–glycerine and air–water systems, as shown in Figure 3 for column C. In both injector systems, bubbles are simultaneously injected into the flow domain at a time interval (t_B) of 0.18 s for the two-bubble injector case and at a time interval (t_B) of 0.10 s for the three-bubble injector case. The initial bubble diameter for all cases is 0.5 cm. A typical time step for the computations is 3.0×10^{-4} s. The computations are run for about ten CRAY CPU hours for each condition to yield the complete dynamic characteristics of the system.

Air–Glycerine System. For air bubbles in 80 wt. % glycerine solution, Figures 20 and 21 show the computational results together with experimental results from the PIV and photographs of the experimental system in the two different injector setups. The computational conditions precisely match the experimental conditions regarding system dimensions, height-to-width ratio, bubble injector locations, and bubble frequency. In Figure 20, the time interval between the lower two frames is approximately 1/10 s for all three sets of data shown, while the time interval between the middle and top frames is approximately 1/15 s. The time interval between each frame shown in Figure 21 is about 1/15 s for all three sets of data. From Figures 20 and 21, it can be seen that the computations demonstrate a relatively stable flow pattern through the liquid velocity vectors and by the observation that no pressure gradients are seen to exist in the x direction. The pressure drop between two adjacent pressure contour lines shown in the computational results is approximately 97 N/m^2. The bubble size and shape are also seen to remain uniform throughout the column. The overall averaged flow patterns observed from both the computation and PIV results are shown in Figure 22. The liquid ascends in the region close to the bubble chains and descends between two bubble chains and near the sidewalls. Based on such flow patterns, it can be seen that there are four and six circulation cells in the two- and three-bubble injector cases, respectively. The bottom corners of the column are observed to be relatively stagnant regions.

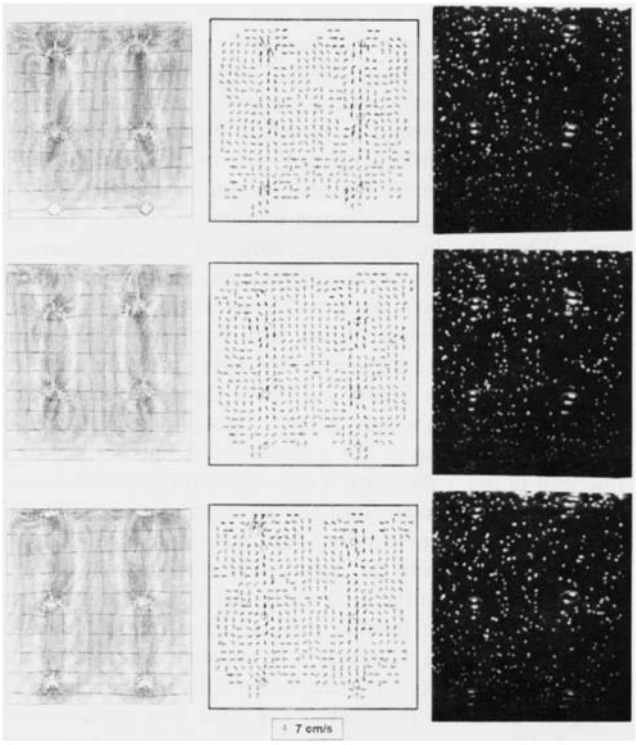

Figure 20. Comparison of computational results, PIV results and photographs taken from experimental setup for air–glycerine system in two-bubble injector case ($U_1 = 0$, $t_B = 0.18$ s).

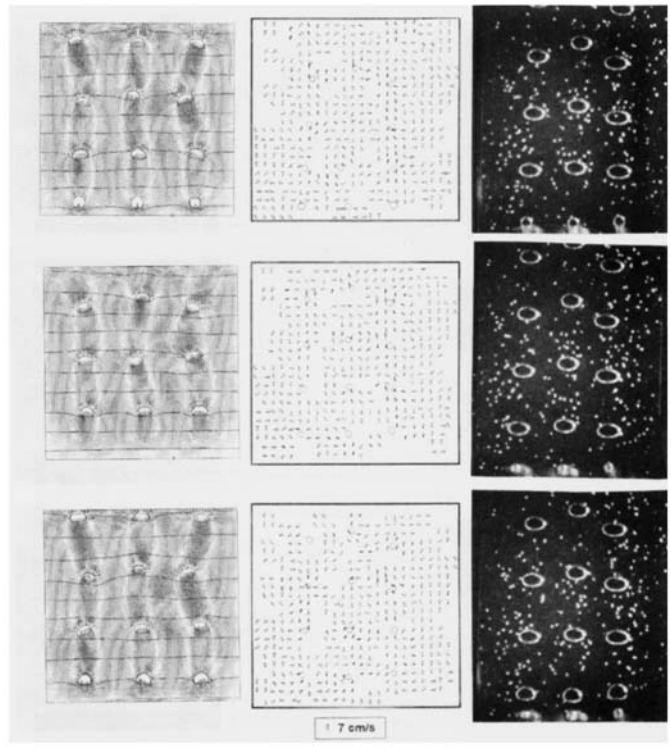

Figure 21. Comparison of computational results, PIV results and photographs taken from experimental setup for air–glycerine system in three-bubble injector case ($U_1 = 0$, $t_B = 0.1$ s).

The instantaneous phenomena provided by the computations and the PIV results show that there are two vortices located beneath each bubble, illustrating the wake region. The simulations demonstrate the wake motion beneath each bubble but show no signs of wake shedding, which is confirmed by the PIV results by showing that the only vortices present are in the wake region directly beneath the bubbles. Therefore, in both the two- and three-injector cases the bubbles rise upward in a rectilinear manner with no rocking motion. Vortices observable just below the free surface are the result of bubbles that have left the free surface coupled with the overall motion of the liquid phase discussed earlier.

The flow phenomena obtained from the computations exhibit the same qualitative trends as observed from flow visualization and the PIV results. In order to ascertain the accuracy of the computational results, several local liquid velocities and vortex sizes below the free surface are used to compare between the computational and experimental results. The local liquid velocities obtained from the computational and PIV results for a region in front of the bubbles are within 5% of each other. The vortex sizes below the free surface are about 0.5 cm in both the experimental and computational results. Figures 20 and 21 demonstrate that the computational technique is able to qualitatively and quantitatively simulate the air–glycerine dispersed bubbly flow quite accurately.

Air–Water System. Based on the results obtained in the air–glycerine system, the computations are extended to simulate air–water dispersed bubbly flow using the same geometrical parameters given previously. Figure 23 shows three representative examples of the computational results together with the PIV results and the photographs of the experimental flow system for the two-bubble injector case. The three frames in Figure 23 are separated by 1/15 s. The computational results demonstrate, as expected, that the air–water flow is much more transient than the air–glycerine case. Pressure gradients are seen to exist not only in the z direction but also the x direction for the air–water flow. The pressure difference between two pressure contour lines from the computa-

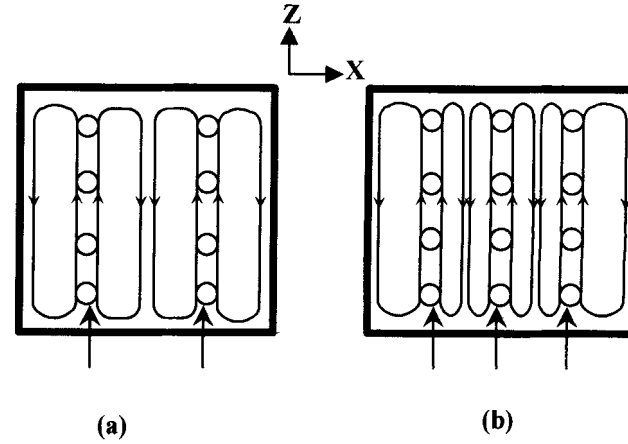

Figure 22. Overall flow pattern of the air–glycerine system in two- ($U_1 = 0$, $t_B = 0.1$ s) and three-bubble injector cases ($U_1 = 0$, $t_B = 0.1$ s).

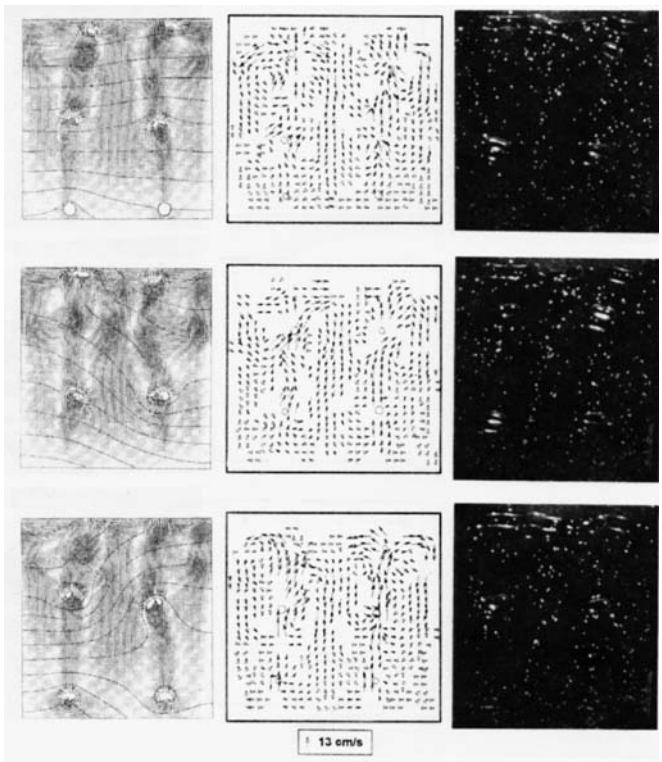

Figure 23. Comparison of computational results, PIV results, and photographs taken from experimental setup for air–water system in two-bubble injector case ($U_1 = 0$, $t_B = 0.18$ s).

tional results is about 82 N/m^2. The bubbles are observed to be more ellipsoidal in shape than in the glycerine system and are observed to be of similar shape in the simulation results and in the photographs taken from the experimental setup. The bubbles are seen to change shape as well as direction throughout the column due to the complicated nature of the pressure field. The overall averaged flow pattern is similar to that of the air–glycerine system in the two-bubble injector case with the liquid rising in the vicinity of the bubbles and descending along the sidewalls and in the middle of the column. The bottom corners of the flow field are again observed to be quite stagnant.

In the air–glycerine system, vortices only exist beneath the bubbles and below the free surface. In the air–water system, however, wake or vortex shedding is observed to occur behind the rising bubbles, as shown in Figure 24. The vortex shedding causes the bubbles to move upward in a zigzag pattern, introducing strong interactions between the existing liquid flow field and the bubble motion. A vortex that has been shed becomes a part of the local, transient flow pattern. This local flow pattern or structure then directly affects the motion as well as the vortex shedding of the following bubbles. The new local flow structure created by the shed vortex can be reinforced or destroyed during its interaction with the following bubbles. In the former case the new local structure can grow into a large coherent flow structure in the bubble column such as the vortices in the vortical flow region discussed previously, while in the latter case the structure is dissipated into the surrounding flow. Since the vortex shedding process is transient in nature and every shed vortex introduces a new change in the flow field, the overall dispersed bubbly flow becomes unstable and highly transient.

In the three-injector case, the interaction between the bubbles becomes enhanced as shown in Figure 25. The bubbles in this case are influenced not only by the leading bubble from the same injector but also by leading bubbles from the other injectors and by adjacent bubbles injected at the same time. When the bubbles come within a certain distance of each other, as in the three-injector case, the bubble motion is affected by the lower pressure known to exist in the wake of the surrounding bubbles (Fan and Tsuchiya, 1990) causing the bubble to accelerate toward the lower pressure area. This is demonstrated in Figure 26, where the wake effects influence the bubbles not only in the z direction as in the two-injector case, but also in the x direction. A bubble may be influenced in the x direction if one of the three simultaneously injected bubbles slows down slightly causing it to fall into the wake of an adjacent bubble. This can result in a change of the bubble shape and the bubble will accelerate in the x direction as well as in the z direction due to the lower pressure in the wake of the leading bubble. This transient behavior causes the pressure distribution to become more complicated and the numerical convergence more difficult to achieve.

Figure 27 shows the overall averaged flow pattern of the three-bubble injector case. It can be seen that the bubbles rise in the center of the column carrying the liquid upward in this region. Due to the mass conservation of the liquid phase, the direction of the liquid motion near the top of the column shifts toward the sidewalls and at the bottom of the column the liquid motion is directed toward the center. This liquid motion forms the overall liquid circulating motion and produces two circulation cells in the flow field. The bubbles tend

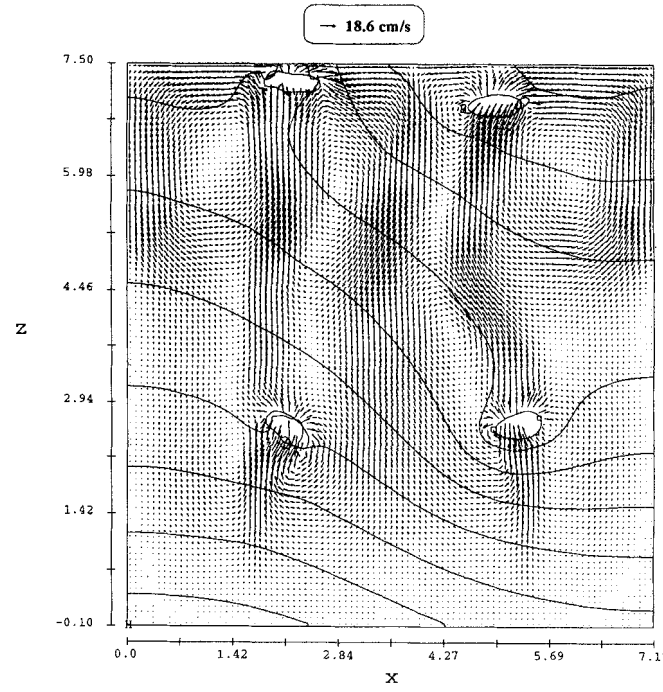

Figure 24. Example of the computational results for the two-bubble injector case air-water system ($U_1 = 0$, $t_B = 0.18$ s).

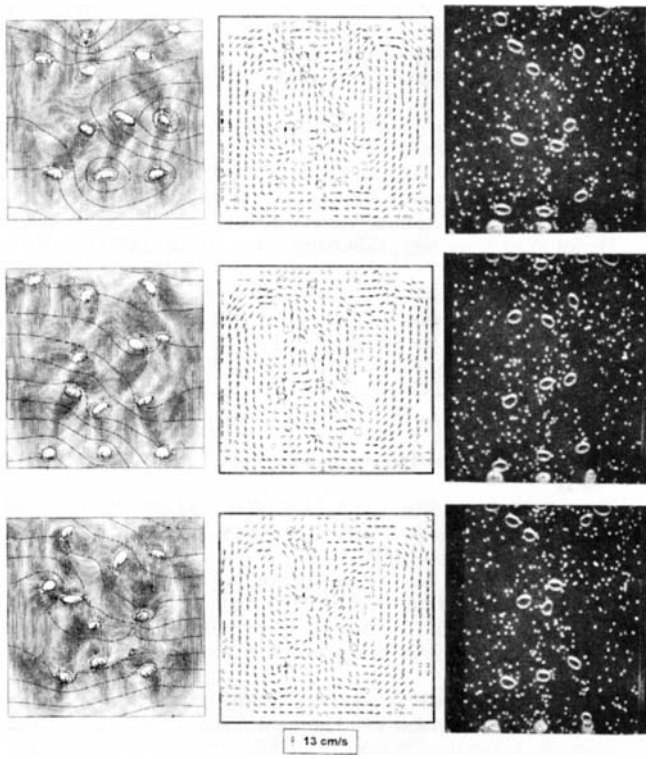

Figure 25. Comparison of computational results, PIV results, and photographs taken from experimental setup for air–water system in three-bubble injector case ($U_1 = 0$, $t_B = 0.1$ s).

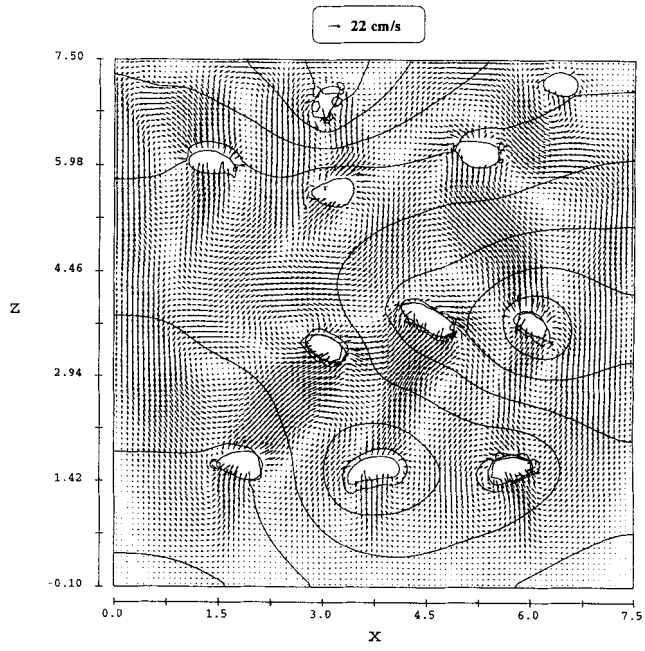

Figure 26. Example of the computational results for the three-bubble injector case air–water system ($U_1 = 0$, $t_B = 0.1$ s).

to follow the liquid motion resulting in the familiar cooling tower bubble distribution in the z direction (Field, 1981). The wake effects of the leading bubbles influence the trailing bubbles adequately to further reinforce the cooling tower motion but not enough to cause any bubble coalescence.

The instantaneous phenomena of the air–water simulation (Figures 23 and 25) associated with the bubble wake motion is much more pronounced than previously observed for the air–glycerine system (Figures 20 and 21). As shown in Figure 27, at the neck of the cooling tower, bubbles are so close that some of the vortices created by different bubbles may interact with each other and enhance the vortex shedding from the bubble, or may interfere with each other to cancel the vortical liquid motion. Therefore, in this region the fluid motion is highly irregular and transient. These qualitative results are confirmed from the data provided by the PIV technique and from flow visualization of the experimental system.

From the PIV data shown in Figures 23 and 25, the vortices are observed to be more random and larger than in the air–glycerine case. In the two-bubble injector case, the vortex size just beneath the free surface is around 1.78 cm, which is in very good agreement with the experimental value 1.74 cm. Also the large vortex size measured from the experimental results in the three-bubble injector case is about 1.42 cm, which matches the computational results of 1.48 cm very well. For the two-bubble injector case, typical measurements by the PIV system for the local liquid phase velocity near the sidewalls and in front of the bubbles are around 12 cm/s and 22 cm/s, respectively, which compare well with 11.5 and 21 cm/s obtained from the computation. This confirms that the computation for the air–water system is quantitatively comparable with the experimental results.

The results of both the air–glycerine and air–water computations when compared with the experimental data,

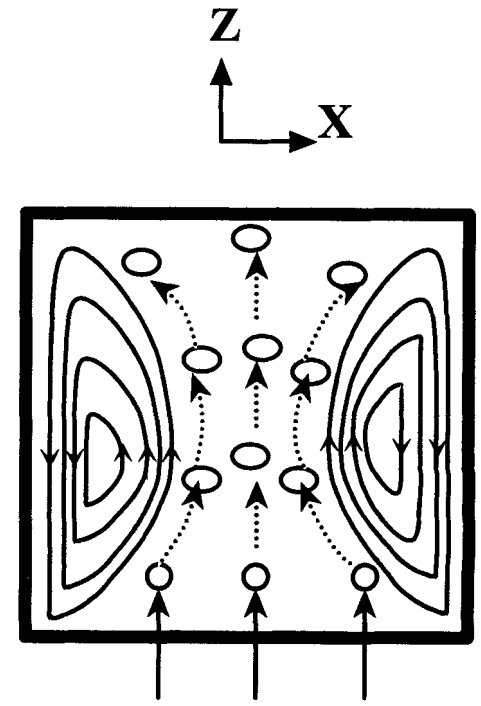

Figure 27. Overall flow pattern of the air–water system in the three-bubble injector case ($U_1 = 0$, $t_B = 0.1$ s).

demonstrate that the VOF method of solution is of promise for further study of larger scale 2-D and 3-D computations. The technique is unique in providing time-dependent flow field information around individual bubbles by tracking the gas–liquid interface without involving assumptions on the gas–liquid momentum transfer. Furthermore, the technique is able to provide insight into the coupling effects of the liquid and bubble motion.

Concluding Remarks

The quantitative analysis based on data obtained using the PIV technique provides insight into the instantaneous flow behavior and regime transition in two-dimensional bubble columns. The analysis indicates that the observed coherent flow structures can be characterized by such macroscopic properties as vortex size and wavelength of the fast bubble flow region. Specifically, the two flow regimes, that is, the dispersed bubble regime and coalesced bubble regime can be demarcated based on the behavior of the vortex size while the variation of the wavelength can differentiate between the 4-region and 3-region flow conditions that underlie the coalesced bubble regime. The behavior of the radial and axial profiles of gas holdup and liquid velocity signifies the differences between the instantaneous and time/volume averaged flow structures and reflects the scale effects on the regime transition. Numerical simulations of dispersed bubbly flows are conducted based on the VOF method. The computational results indicate the unsteady nature of the flow due to the coupling effects of the pressure field, liquid velocity, and bubble motion. The numerical results compare well both qualitatively and quantitatively with the experimental results obtained by the PIV technique and from flow visualization.

Acknowledgment

This work was supported by National Science Foundation grant CTS-9200793 and by the Ohio Supercomputer Center.

Notation

d_p = particle diameter (cm)
D = column width (cm)
U_l = superficial liquid velocity (cm/s)
U_g = superficial gas velocity (cm/s)
ρ_s = solid density (g/cm^3)

Literature Cited

Boris, J. P., "New Directions in Computational Fluid Dynamics," *Annu. Rev. Fluid Mech.*, **21**, 345 (1989).
Celik, I., and Y.-Z. Wang, "Numerical Simulation of Circulation in Gas-Liquid Column Reactors: Isothermal, Bubbly, Laminar Flow," *Int. J. Multiphase Flow*, **20**, 1053 (1994).
Chen, J. J. J., M. Jamialahmadi, and S. M. Li, "Effect of Liquid Depth on Circulation in Bubble Columns: A Visual Study," *Chem. Eng. Res. Des.*, **67**, 203 (1989).
Chen, R. C., and L.-S. Fan, "Particle Image Velocimetry for Characterizing the Flow Structure in Three-Dimensional Gas-Liquid-Solid Fluidized Beds," *Chem. Eng. Sci.*, **47**, 3615 (1992).
Chen, R. C., J. Reese, and L.-S. Fan, "Flow Structure in a Three-Dimensional Bubble Column and Three-Phase Fluidized Bed," *AIChE J.*, **40**, 1093 (1994).
De Nevers, N., "Bubble Driven Fluid Circulations," *AIChE J.*, **14**, 222 (1968).
Deckwer, W. D., and A. Schumpe, "Bubble Columns—The State of Art and Current Trend," *Int. Chem. Eng.*, **27**, 405 (1987).
Devanathan, N., D. Moslemian, and M. P. Dudukovic, "Flow Mapping in Bubble Columns Using CARPT," *Chem. Eng. Sci.*, **45**, 2285 (1990).
Fan, L.-S., *Gas-Liquid-Solid Fluidization Engineering*, Butterworth, Stoneham, MA (1989).
Fan, L.-S., and K. Tsuchiya, *Bubble Wake Dynamics in Liquid and Liquid-Solid Suspensions*, Butterworth, Stoneham, MA (1990).
Field, R. W., 8th Annual Research Meeting, Trans. IChemE., Heriot-Watt University, Edinburgh (Apr. 27–28, 1981) (quoted by Chen et al., 1989).
Franz, K., T. Borner, H. J. Kantorek, and R. Buchholz, "Flow Structures in Bubble Columns," *Ger. Chem. Eng.*, **7**, 365 (1984).
Freedman, W., and J. F. Davidson, "Hold-up and Liquid Circulation in Bubble Columns," *Trans. IChemE.*, **47**, T251 (1969).
Geary, N. W., and R. G. Rice, "Circulation and Scale-Up in Bubble Columns," *AIChE J.*, **38**, 79 (1992).
Harlow, F. H., and J. E. Welch, "Numerical Calculations of Time-Dependent Viscous Incompressible Flow," *Phys. Fluids*, **8**, 2182 (1965).
Harper, R. P., C. W. Hirt, and J. M. Sicilian, "FLOW-3D: Computational Modeling Power for Scientists and Engineers," *Flow Science, Inc.*, Rep. FSI-91-00-1 (1991).
Hills, J. H., "Radial Non-Uniformity of Velocity and Voidage in a Bubble Column," *Trans. IChemE.*, **52**, 1 (1974).
Hirt, C. W., and B. D. Nichols, "Volume of Fluid (VOF) Method for the Dynamics of Free Boundaries," *J. Comput. Physics*, **39**, 201 (1981).
Hirt, C. W., B. D. Nichols, and N. C. Romero, "SOLA—A Numerical Solution Algorithm for Transient Fluid Flows," Los Alamos Scientific Laboratory Report LA-5852 (1975).
Lapin, A., and A. Lübbert, "Numerical Simulation of the Dynamics of Two-Phase Gas-Liquid Flows in Bubble Columns," *Chem. Eng. Sci.*, **49**, 3661 (1994).
Miyauchi, T., and C.-N. Shyu, "Flow of Fluid in Gas-Bubble Columns," *Kagaku Kogaku*, **34**, 958 (1970).
Muroyama, K., and L.-S. Fan, "Fundamentals of Gas-Liquid-Solid Fluidization," *AIChE J.*, **31**, 1 (1985).
Reese, J., R. C. Chen, J.-W. Tzeng, and L.-S. Fan, "Characterization of the Macroscopic Flow Structure in Gas-Liquid and Gas-Liquid-Solid Fluidization Systems Using Particle Image Velocimetry," *Int. Video J. Eng. Res.*, **3**, 17 (1993).
Shah, Y. T., B. G. Kelkar, S. P. Godbole, and W. D. Deckwer, "Design Parameters Estimations for Bubble Column Reactors," *AIChE J.*, **28**, 353 (1982).
Sokolichin, A., S. Becker, and G. Eigenberger, "Modellierung und Numerische Simulation von G/L-Blasen-Strömungen," *Chem. Eng. Techn.*, **66**, 505 (1993).
Svendsen, H. F., H. A. Jakobsen, and R. Torvik, "Local Flow Structures in Internal Loop and Bubble Column Reactors," *Chem. Eng. Sci.*, **47**, 3297 (1992).
Tarmy, B. L., and C. A. Coulaloglou, "Alpha-Omega and Beyond Industrial View of Gas/Liquid/Solid Reactor Development," *Chem. Eng. Sci.*, **47**, 3231 (1992).
Tzeng, J.-W., R. C. Chen, and L.-S. Fan, "Visualization of Flow Characteristics in a 2-D Bubble Column and Three-Phase Fluidized Bed," *AIChE J.*, **39**, 733 (1993).
Ulbrecht, J. J., Y. Kawase, and K. F. Auyeung, "More on Mixing of Viscous Liquid in Bubble Columns," *Chem. Eng. Commun.*, **35**, 175 (1985).
Walter, J. F., and H. W. Blanch, "Liquid Circulation Patters and Their Effect on Gas Hold-Up and Axial Mixing in Bubble Columns," *Chem. Eng. Commun.*, **19**, 243 (1983).
Webb, C., F. Que, and P. R. Senior, "Dynamic Simulation of Gas-Liquid Dispersion Behavior in a 2-D Bubble Column Using a Graphics Mini-Supercomputer," *Chem. Eng. Sci.*, **47**, 3305 (1992).
Yang, Z., U. Rustemeyer, R. Buchholz, and U. Onken, "Profile of Liquid Flow in Bubble Columns," *Chem. Eng. Commun.*, **49**, 51 (1986).

Manuscript received Sept. 16, 1994, and revision received Apr. 6, 1995.